

# Bifacial Wide-Gap (Ag,Cu)(In,Ga)Se<sub>2</sub> Solar Cell with 13.6% Efficiency Using In<sub>2</sub>O<sub>3</sub>:W as a Back Contact Material

Jan Keller,\* Lars Stolt, Olivier Donzel-Gargand, André F. Violas, Tomas Kubart, and Marika Edoff

This study evaluates In<sub>2</sub>O<sub>3</sub>:W as a transparent back contact material in wide-gap (bandgap range = 1.44–1.52 eV) (Ag,Cu)(In,Ga)Se<sub>2</sub> (ACIGS) solar cells for potential application as a top cell in a tandem device. High silver concentrations and close-stoichiometric absorber compositions result in a complete depletion of free charge carriers, allowing for decent electron collection, despite the low diffusion length. Remarkable efficiencies of 13.6% and 7.5% are reached using 1 μm- and 400 nm-thick absorbers, respectively. At rear illumination (i.e., superstrate backwall), the best cell shows an efficiency of 8.7%. For each of the four analyzed samples, the short-circuit current at rear illumination reaches at least 60% of the value at front illumination. Losses arise from recombination at the back contact and a too low drift/diffusion length. The parasitic absorption by the transparent electrodes for photon energies close to the bandgap of a potential Si bottom cell (1.1 eV) is close to 15%. Strategies to reduce this value and to further increase the efficiency are discussed.

a Si (or even another ACIGS) bottom cell, its bandgap needs to be at least 1.4 eV.<sup>[3,4]</sup> This requires ACIGS compositions with substantially higher [Ga]/([Ga]+[In]) (GGI) ratios than implemented in the best low-gap cells with GGI ≤ 0.3.<sup>[1]</sup> For GGI > 0.3, the absorber bulk quality deteriorates with increasing Ga content and decreasing electron lifetimes result in lower diffusion lengths and thus, worsening carrier collection and higher open circuit voltage (V<sub>OC</sub>) deficits.<sup>[5–16]</sup> When the GGI is increased above 0.5, recombination at the interface with a standard CdS buffer layer is suggested to act as an additional V<sub>OC</sub> limitation, because a detrimental negative conduction band offset (CBO) is created.<sup>[17–19]</sup> However, by alloying sufficiently high concentrations of Ag to the absorber, a negative CBO can be

## 1. Introduction

Solar cells based on the chalcopyrite absorber material (Ag,Cu)(In,Ga)Se<sub>2</sub> (ACIGS) have reached efficiencies of up to 23.6%.<sup>[1]</sup> The highest efficiencies are typically achieved for bandgap (E<sub>G</sub>) values close to 1.1 eV,<sup>[1,2]</sup> matching the E<sub>G</sub> of Si. To make an ACIGS solar cell suitable for a top cell in a tandem device with

avoided<sup>[20–22]</sup> and V<sub>OC</sub> losses mitigated.<sup>[5,22–28]</sup> Previous calculations predict that for [Ag]/([Ag]+[Cu]) (AAC) ratios ≥ 0.8, the CBO to CdS is positive for all ACIGS compositions, i.e., even for GGI = 1.<sup>[22]</sup> Besides reducing the energetic positions of the ACIGS band edges, Ag-alloying also leads to a continuous increase in E<sub>G</sub> for AAC ≥ 0.5 for all Ga contents.<sup>[22,29,30]</sup>

In this work, we add a high silver concentration of AAC ≈ 0.8 to the absorber, which allows to reach E<sub>G</sub> values of about 1.5 eV, while staying below a GGI value of 0.6. The intention is to minimize fill factor (FF) and V<sub>OC</sub> losses as much as possible, which, according to our earlier works, are increasingly dominant for GGI > 0.7.<sup>[28]</sup> In addition, only very close-stoichiometric absorbers with ([Ag]+[Cu])/([In]+[Ga]) = [I]/[III] ≈ 0.9–1.0 were produced in this work. Previous studies on wide-gap ACIGS solar cells have shown that the net free carrier density drastically reduces when approaching stoichiometric composition for absorbers with AAC ≥ 0.4.<sup>[5,31,32]</sup> Thus, by fabricating close-stoichiometric ACIGS films, the space charge region (SCR) width (W<sub>SCR</sub>) is extended, improving the otherwise low short-circuit current density (J<sub>sc</sub>) of the wide-gap solar cells. Facilitating the collection efficiency for carriers generated close to the (nominal) back electrode becomes of paramount importance when the device is illuminated from the rear side, which of course requires the utilization of a transparent back contact (TBC).


Different n-type transparent conductive oxide (TCO) materials, such as SnO<sub>2</sub>:F (FTO),<sup>[33–40]</sup> ZnO:Al (AZO),<sup>[34,37,41–43]</sup> In<sub>2</sub>O<sub>3</sub>:Sn (ITO),<sup>[34,38,40,43–57]</sup> and In<sub>2</sub>O<sub>3</sub>:H (IOH)<sup>[58–60]</sup> were tested as back contact layers for (A)CIGS solar cells. However,

J. Keller, L. Stolt, O. Donzel-Gargand, M. Edoff  
Ångström Laboratory  
Division of Solar Cell Technology  
Uppsala University  
75121 Uppsala, Sweden  
E-mail: jan.keller@angstrom.uu.se

A. F. Violas  
International Iberian Nanotechnology Laboratory  
Avenida Mestre José Veiga, 4715-330 Braga, Portugal

A. F. Violas  
Physics Department  
Aveiro University  
Campus Universitário de Santiago, 3810-193 Aveiro, Portugal

T. Kubart  
Ångström Laboratory  
Division of Solid-State Electronics  
Uppsala University  
75121 Uppsala, Sweden

 The ORCID identification number(s) for the author(s) of this article can be found under <https://doi.org/10.1002/solr.202400430>.

DOI: 10.1002/solr.202400430

to use the device as a top cell in a tandem structure, it should allow for a very high optical transmission for photon energies between the bandgap values of the top and bottom cells. In the case of a Si bottom cell, this would require a high near-infrared (NIR) transmission up to a wavelength ( $\lambda$ ) of about 1150 nm. Since only the front and back electrodes of our ACIGS solar cell structure absorb in this spectral range via free charge carrier absorption, it is of uttermost importance to reduce the concentration of electrons  $n$  in those layers ( $n < 2 \times 10^{20} \text{ cm}^{-3}$ ). At the same time, a sufficiently high lateral conductivity needs to be assured (i.e., low sheet resistance ( $R_{\text{sheet}}$ )), which is only given for high mobility ( $\mu$ ) TCOs, without substantially increasing the layer thickness. Thus, of all the abovementioned TCO candidates, only  $\text{In}_2\text{O}_3:\text{H}$  ( $\mu > 130 \text{ cm}^2 \text{ Vs}^{-1}$  and  $n < 2 \times 10^{20} \text{ cm}^{-3}$  after solid-phase crystallization<sup>[61]</sup>) seems suitable as a back (and also front) contact material in an ACIGS top cell. Indeed, very low NIR absorption in the  $\text{In}_2\text{O}_3:\text{H}$  back contact was observed in one of our recent works on wide-gap ACIGS solar cells.<sup>[60]</sup> A drawback of using IOH is that the conductivity is decreasing for annealing temperatures  $> 300^\circ\text{C}$ , due to a strong reduction in  $n$ .<sup>[62]</sup> As a consequence, the sheet resistance ( $R_{\text{sheet}}$ ) increased by a factor of 2–4 after absorber deposition at a temperature  $> 500^\circ\text{C}$ .<sup>[58–60]</sup> Furthermore, the sputter process to fabricate high-quality IOH films is rather complex (e.g., requires accurate  $\text{H}_2/\text{H}_2\text{O}$  partial pressure control<sup>[61]</sup>) and time-consuming. Thus, the present work, for the first time, evaluates  $\text{In}_2\text{O}_3:\text{W}$  (IOW) as a TBC in a wide-gap ACIGS cell. Koida et al. have shown before that polycrystalline IOW films grown at  $200^\circ\text{C}$  are very stable (even improve) up to annealing temperatures of  $500^\circ\text{C}$ , exhibiting a mobility of  $\mu \approx 120 \text{ cm}^2 \text{ Vs}^{-1}$  and  $n < 2 \times 10^{20} \text{ cm}^{-3}$  after annealing.<sup>[62]</sup> In this study, the IOW TBCs are sputtered at room temperature, which was reported to also result in decent electro-optical properties,<sup>[63–66]</sup> to allow for faster processing and higher throughput. Gan et al. found that amorphous IOW layers sputtered at room temperature crystallized upon annealing temperatures  $> 150^\circ\text{C}$  and they reported very high  $\mu \approx 120 \text{ cm}^2 \text{ Vs}^{-1}$  and low  $n \approx 1.7 \times 10^{20} \text{ cm}^{-3}$  values after annealing for 15 min at  $200^\circ\text{C}$ . However, the stability of amorphous IOW films

subjected to temperatures  $> 500^\circ\text{C}$  (as reached during ACIGS deposition) was, to the best of our knowledge, not tested before.

## 2. Results and Discussion

Four 3-stage coevaporation process runs were conducted to deposit ACIGS absorbers with different thicknesses  $d_{\text{ACIGS}}$ , but similar compositions. The corresponding compositional ratios AAC, GGI, and [I]/[III], as determined by X-ray fluorescence (XRF), and the resulting  $E_G$  values (from external quantum efficiency (EQE) inflection point) are shown in **Table 1**. The bandgap varies between 1.44 and 1.52 eV for the samples in this study.

Two very thin absorbers, with  $d_{\text{ACIGS}} \approx 400 \text{ nm}$  and  $\approx 450 \text{ nm}$ , and two thicker absorbers, both with  $d_{\text{ACIGS}} \approx 1 \mu\text{m}$ , were processed on top of NaF-coated IOW TBCs and simultaneously on reference samples with a standard opaque Mo back contact (soda lime glass (SLG) used as substrates). One of the IOW samples with the thicker absorber (labeled run 4 in Table 1) has a slightly higher [I]/[III] value than the other one (labeled run 3 in Table 1), [I]/[III] = 0.94 versus 0.90, potentially explaining performance differences.

### 2.1. Chemical and Microstructural Analysis of the Solar Cells

The cross-section images, obtained from scanning electron microscopy (SEM), of the complete solar cell stacks with IOW as a back contact are illustrated in **Figure 1** for the samples with the 400 nm- and  $1 \mu\text{m}$ -thick (run 1 and run 4, respectively) absorbers. A CdS layer is used as a buffer and AZO ( $R_{\text{sheet}} = 40 \Omega \text{ sq}^{-1}$ ) acts as the front electrode. The as-grown IOW films have a sheet resistance of  $\approx 11 \Omega \text{ sq}^{-1}$  at a thickness of 300 nm (i.e., resistivity  $\approx 3.3 \times 10^{-4} \Omega \text{ cm}$ ). After absorber deposition,  $R_{\text{sheet}}$  increases to  $45 \Omega \text{ sq}^{-1}$  in the final device. The origin of this degradation will be discussed in more detail below. Due to the shorter processing time, the grain size of the thinner absorber is smaller, leading to reduced surface roughness.

**Table 1.** Absorber properties and corresponding JV parameters (best cells) for all four samples processed in this study. The JV parameters are shown for front and rear illumination for samples with an IOW back contact. The value in brackets is the percentage of  $J_{\text{SC,EQE}}$  reached at the rear in relation to front illumination.

$d_{\text{ACIGS}}$ [nm]	Back contact	GGI	AAC	[I]/[III]	$E_G$ [eV]	FF [%]	$V_{\text{OC}}$ [mV]	$J_{\text{SC,IV}}$ [ $\text{mA cm}^{-2}$ ]	$J_{\text{SC,EQE}}$ [ $\text{mA cm}^{-2}$ ]	$\eta_{\text{IV}}$ [%]	$\eta_{\text{EQE}}$ [%]
400 (run 1)	Mo	0.55	0.79	0.90	1.51	70.7	799	17.4	15.5	9.8	8.8
	IOW front/rear	0.55	0.79	0.96	1.52	61.4/49.8	817/771	16.6/10.5	14.9/9.0 (60%)	8.3/4.0	7.5/3.5
450 (run 2)	Mo	0.56	0.80	0.92	1.51	67.4	794	17.5	15.0	9.4	8.0
	IOW front/rear	0.56	0.80	0.90	1.52	57.9/41.0	795/604	17.3/11.8	16.1/10.7 (66%)	8.0/2.9	7.4/2.6
1000 (run 3)	Mo	0.58	0.81	0.94	1.46	77.1	858	22.3	21.2	14.8	14.0
	IOW front/rear	0.58	0.81	0.91	1.46	71.5/73.1	843/815	22.9/10.5	21.7/13.1 (60%)	13.8/6.3	13.1/7.8
1000 (run 4)	Mo	0.59	0.81	0.88	1.46	77.1	854	22.2	21.5	14.6	14.2
	IOW front/rear	0.57	0.82	0.94	1.44	70.8/75.8	853/824	23.2/12.1	22.5/14.0 (62%)	14.0/7.6	13.6/8.7

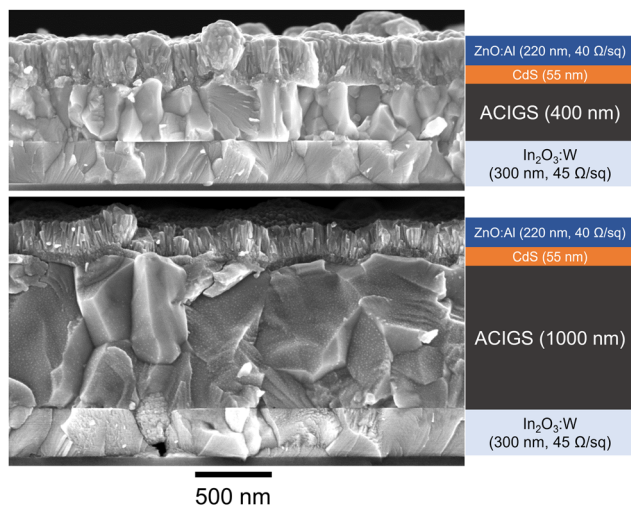


**Figure 1.** Cross-section SEM images of the sample with a 400 nm- (top, run 1) and with a 1 μm-thick (bottom, run 4) ACIGS absorber. The scale bar refers to both images.

For all samples, a GGI grading was implemented to reduce the number of electrons 1) generated close to and 2) diffusing toward the back contact. A previous study on low-gap, bifacial ACIGS solar cells highlights how a very confined, steep increase in Ga concentration toward the back contact can effectively improve the carrier collection at rear illumination.<sup>[67]</sup> The laterally averaged (area ≈ 3 mm<sup>2</sup>) AAC and GGI depth profiles of the 1 μm-thick sample (run 4), obtained from glow-discharge optical emission spectroscopy (GDOES), are displayed in **Figure 2**.

The upper half of the absorber shows a rather constant GGI of ≈ 0.54. Toward the back contact, the value increases, reaching GGI ≈ 0.68 at the interface to IOW. No sudden, abrupt increase in GGI is detected in the direct vicinity of the ACIGS/IOW interface, suggesting that an excessive GaO<sub>x</sub> formation could be avoided.<sup>[60]</sup> The AAC value remains rather constant across the entire absorber depth. In earlier works on wide-gap ACIGS,

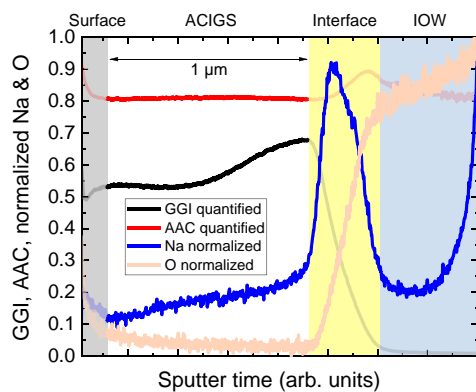


**Figure 2.** Depth profiles of the AAC and GGI ratios as determined by GDOES (quantified according to integral XRF-deduced compositions). The normalized sodium and oxygen profiles are shown, too. An adequate quantification of the absorber composition can only be provided for sputter depths, at which the GDOES signal does not contain elements from different layers/phases at the surface and back interface (white area).

an anticorrelation of the GGI and AAC profiles was observed.<sup>[22]</sup> This feature is less pronounced here, due to the rather low GGI and its moderate depth variation as well as the high AAC level. The thermodynamically-driven instability, which causes the mentioned anticorrelation, is highest for AAC ≈ 0.5 and GGI → 1.<sup>[68]</sup> Figure 2 also shows the normalized Na and O profiles. Sodium diffusion from the SLG into the bottom part of the IOW is visible. However, the majority of the sodium in the absorber and at its interfaces stems from the NaF-precursor (In<sub>2</sub>O<sub>3</sub>-based TCOs do not allow for sufficient in-diffusion of Na from the SLG). A strong accumulation of Na is found at the absorber/TBC interface. Inside the absorber, the Na concentration decreases toward the surface, presumably due to the higher grain boundary density in the bottom part.<sup>[69]</sup> At the very surface, the Na and O signals increase again, indicating the presence of very thin surface phases (i.e., oxidation products).<sup>[70]</sup>

It was suggested before that an excessive GaO<sub>x</sub> formation at the absorber/TBC interface creates a barrier for hole extraction and may even result in a reduced electron collection, due to a local reversal of the GGI profile.<sup>[58–60]</sup> To identify a possible GaO<sub>x</sub> formation at the ACIGS/IOW interface (not detected in GDOES), scanning transmission electron microscopy (STEM) analysis assisted by energy-dispersive X-ray spectroscopy (EDS) was conducted on the sample with the 400 nm-thick absorber. The corresponding STEM images of the complete device (bright field) and the back contact interface (bright and dark field) are illustrated in **Figure 3a–c**, respectively. A very thin GaO<sub>x</sub> layer (measured to 1.5 nm) is found, which is much thinner than usually reported for chalcopyrite solar cells on In<sub>2</sub>O<sub>3</sub>-based TBCs.<sup>[58–60]</sup> The reason for the only minor GaO<sub>x</sub> formation is probably that only a very small amount of NaF was added in this study (5 nm NaF-precursor) since the presence of Na was suggested to catalyze GaO<sub>x</sub> formation.<sup>[58,60]</sup> Also, it can be suspected that the larger thermal budget during the growth of the 1 μm-thick absorbers led to slightly thicker GaO<sub>x</sub> interlayers. Moreover, lattice planes are visible in the crystalline absorber and in the IOW film, while the GaO<sub>x</sub> layer appears to be amorphous.

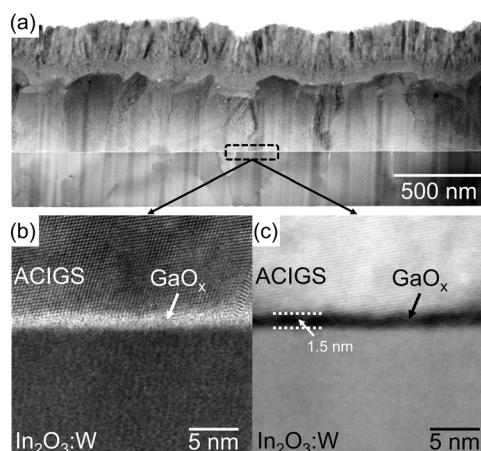


**Figure 3.** a) STEM bright-field image of the complete device with a 400 nm-thick absorber (run 1) as well as higher magnified b) bright-field and as c) dark-field images of the corresponding back contact region.

Figure S1 (Supporting Information), shows the STEM image and the corresponding elemental distributions across a different position at the back interface. The formation of  $\text{GaO}_x$  is clearly confirmed (drop in In and O signals shifted by about 1 nm). Figure S2 (Supporting Information), provides the same analysis for the complete device structure. It is obvious that Ag-depleted ordered vacancy compounds (OVCs) were formed at the surface, although the absorber has a quite close-stoichiometric composition. This is in-line with earlier findings, showing that already for very small group-I deficiency, a substantial amount of OVCs is forming for ACIGS with  $\text{AAC} \geq 0.8$ ,<sup>[26,71,72]</sup> due to the narrowing single-phase region with increasing Ag content.<sup>[73,74]</sup> The GGI grading (measured at a position without a (Ga-enriched) OVC patch) is rather linear and less steep, which is deemed inferior to the GGI grading implemented in the 1  $\mu\text{m}$ -thick absorber layer.

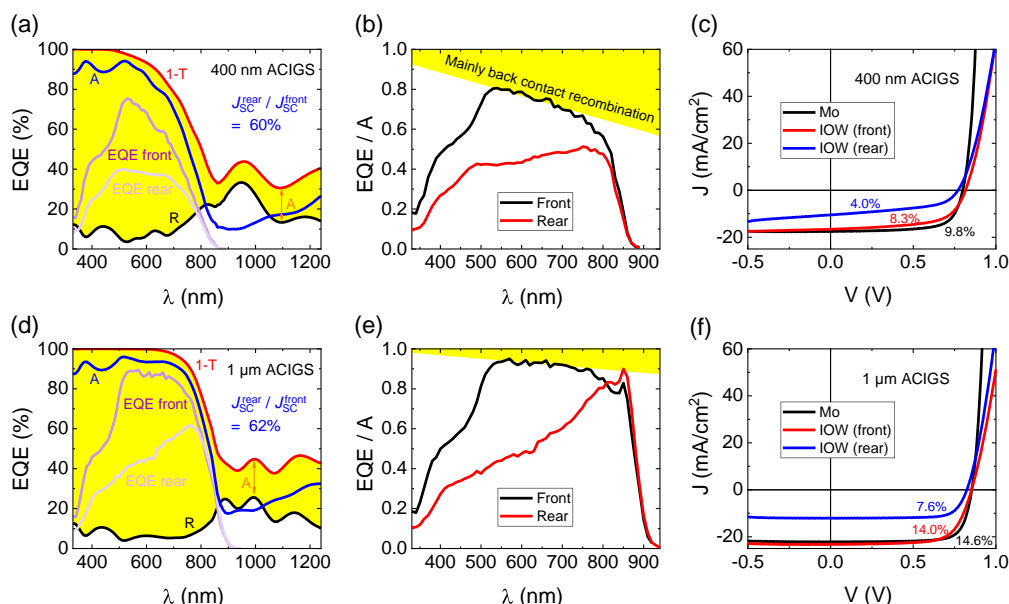
## 2.2. Electrical and Optical Characterization of the Devices

Figure 4 summarizes the EQE, optical, and current–density versus voltage (JV) analysis of the samples with the 400 nm- and 1  $\mu\text{m}$ -thick (run 4) absorbers. For clarity, only the characteristics of the best cells (out of 16) are shown. The same illustration is provided for the samples with the 450 nm- and 1  $\mu\text{m}$ -thick (run 3) absorbers in Figure S3 (Supporting Information). The results are in good agreement with the ones presented here. An antireflection coating was not applied for any sample in this study.

Figure 4a,d shows the corresponding EQE spectra for front and rear illumination as well as the transmittance ( $T$ ), reflectance ( $R$ ), and absorptance ( $A$ ) measured on the complete device stacks before cell definition. As mentioned above, to use the devices in tandem with a Si bottom cell, they have to exhibit very low

absorption for photon energies between  $E_{G,ACIGS}$  and  $E_{G,Si}$  (i.e.,  $\lambda \approx 1150$  nm). The sample with the thinner absorber shows  $A = 18\%$  at  $\lambda \approx 1150$  nm, while the one with the thicker absorber shows  $A = 28\%$ . Similar values are measured for the other two samples ( $A = 17\%$  and  $24\%$ , see Figure S3, Supporting Information). Since the only parameter that changes between all samples is the absorber thickness, these differences in NIR absorption are not intuitive. We suggest that due to the surface roughness of the ACIGS layer, some of the light is refracted at high enough angles to be laterally out-coupled through the edges of the SLG during the optical measurement. This causes an “artificial” overestimation of the absorption. With increasing absorber thickness, the surface roughness increases, leading to higher measured  $A$  values in the NIR region. Indeed, previous measurements on 2  $\mu\text{m}$ -thick ACIGS absorbers on IOH/SLG (almost no NIR absorption) showed a constant artificial offset in NIR absorption of about 17%.<sup>[60]</sup> Thus, we speculate that the “true absorptance” at the Si bandgap is close to 15% for the devices in this study. The 400 nm-thin samples could even be used as a semitransparent device, with  $T \approx 4\%$  at  $\lambda = 555$  nm (highest human eye sensitivity) and  $T \approx 22\%$  at  $\lambda = 700$  nm (for higher  $\lambda$  the eye sensitivity drops to zero). The  $T$  spectra for all samples, plus a sample with a 930 nm absorber that was not included in this study, are illustrated in Figure S4, Supporting Information, together with a photograph of the final sample in front of reflected sunlight (450 nm absorber).

Turning to the EQE curves, it is obvious that for all samples, the carrier collection is higher at front illumination. This is especially true for short wavelengths, since at rear illumination, the majority of electrons are generated close to the back contact. The larger distance to the heterojunction results in a higher



**Figure 4.** Top row: a) EQE spectra at front and rear illumination for the sample with the 400 nm-thick absorber (run 1) as well as corresponding  $R$ ,  $T$ , and  $A$  spectra measured on the complete device. b) EQE spectra normalized to the absorptance  $A$  for the same device. c) Corresponding JV characteristics of the best cell with an IOW TBC at the front and rear illumination as well as for the Mo reference. Bottom row: d–f) Corresponding results for the sample with the 1  $\mu\text{m}$ -thick absorber (run 4).

recombination probability. Both front- and rear-EQE levels are higher for the sample with the 1  $\mu\text{m}$ -thick absorber, mainly due to lower transmission losses. The ratio of the calculated  $J_{\text{SC}}$  (assuming an AM1.5G spectrum and 1 sun intensity) at rear ( $J_{\text{SC,EQE}}^{\text{rear}}$ ) to front ( $J_{\text{SC,EQE}}^{\text{front}}$ ) illumination is between 60% and 66% for all samples in this study. The individual numbers are listed in Table 1. Of course, a  $> 30\%$  loss in  $J_{\text{SC}}$  is too high to justify using the device in rear illumination for real applications (such as in a 4-terminal tandem device in an inverted configuration with the pn-junction down) and strategies need to be developed to reduce this loss. A possible pathway is to passivate the back contact via introducing a dielectric interlayer like  $\text{Al}_2\text{O}_3$  between the absorber and the TBC<sup>[58]</sup> and/or the implementation of a steeper and more confined Ga grading.<sup>[67]</sup> This will be the content of a future study.

Figure 4b,e shows the corresponding EQE spectra normalized to the respective absorptance values. It has to be mentioned that  $A$  also includes the absorption of the window, buffer, and TBC, which means that the shown curves do not exactly correspond to the internal quantum efficiency (IQE). However, since the parasitic absorption is quite small for  $\lambda = 530\text{--}850\text{ nm}$  ( $\approx 3\text{--}4\%$ , more information below), the assumption of  $\text{EQE}/A \approx \text{IQE}$  is justified as a first approximation in this range. Obviously, the carrier collection at front illumination is higher at all wavelengths for the cell with the thicker absorber. The most likely explanation is a more pronounced back contact recombination with thinner absorbers (electrons hardly reach back contact for 1  $\mu\text{m}$ -thick ACIGS). Additionally, the presence of the observed OVC phases at the heterojunction (see Figure S2, Supporting Information) very likely reduces the carrier collection, too.<sup>[75]</sup> In the case of rear illumination, electrons generated close to the back contact ( $\lambda < 550\text{ nm}$ ) are more likely collected in the thinner absorber, due to the shorter distance to the junction and the stronger electric field (field strength should be roughly twice the value of the thicker absorber). However, for higher wavelengths, producing a more homogeneous electron generation profile throughout the absorber, the collection is better for the samples with the thicker absorber (see all rear-EQE and EQE/ $A$  spectra plotted together in Figure S5, Supporting Information). This implies that even at rear illumination the back contact recombination is still more pronounced for the samples with thinner absorbers, probably due to the smaller absorber volume (i.e., generated electrons more likely to “encounter” back contact).

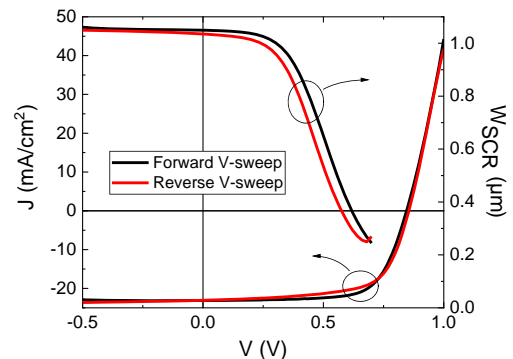
Capacity–voltage (CV) measurements (not shown here) revealed that, as intended, all processed samples are fully depleted (i.e.,  $W_{\text{SCR}} = d_{\text{ACIGS}}$ ) in equilibrium ( $V = 0\text{ V}$ ). The only exception is the Mo reference with the 1  $\mu\text{m}$ -thick (run 4) absorber, showing  $W_{\text{SCR}} \approx 550\text{ nm}$  in equilibrium (positioning of sample caused lowest  $\text{I}/\text{III}$  value of all samples, see Table 1). We believe that the relatively high  $J_{\text{SC,EQE}}^{\text{rear}}$  values for the thicker absorbers could only be reached by facilitating the collection via stretching the electric field through the entire absorber. Otherwise, the low diffusion length of wide-gap ACIGS films would lead to significantly lower  $J_{\text{SC,EQE}}^{\text{rear}}$  values. Still, even for these fully depleted devices, the drift length is seemingly smaller than the absorber thickness. Thus, for perfect/improved collection, a higher absorber quality and implementation of the abovementioned back contact passivation strategies are required.

Figure 4c,f shows the corresponding JV characteristics at front and rear illumination (only front for Mo references). The solar cells with an opaque Mo back contact reach 14.6% and 9.8% efficiency with the thick and thin absorber, respectively. Using IOW as a TBC reduces the efficiency only slightly to 14.0% and 8.3%, respectively, due to a reduction in  $FF$  that mainly arises from the higher  $R_{\text{sheet}}$  of the IOW as compared to Mo ( $R_{\text{sheet}} \approx 0.7\ \Omega\ \text{sq}^{-1}$ ). At rear illumination, the efficiency drops to 7.6% for the thick absorber and 4.0% for the thin absorber. It should be mentioned that the rear-JV was measured about 50 days after the front-JV and that the performance of devices with the thinner absorbers degraded during this period (mainly  $FF$ ).

The light intensity during the JV measurements was adjusted to 1 sun, using a calibrated Si solar cell. The spectral mismatch between the used light source and the AM1.5G spectrum leads to a slight deviation between  $J_{\text{SC,IV}}$  and  $J_{\text{SC,EQE}}$ . Correcting the efficiency only for this difference results in  $\eta_{\text{EQE}} = 14.2\%$  for the Mo reference and  $\eta_{\text{EQE}} = 13.6\%$  (8.7%) for the IOW sample at the front (rear) illumination of the best sample in this study. This is, to the best of our knowledge, the highest efficiency ever reported for a wide-gap ( $E_{\text{G}} > 1.4\text{ eV}$ ) ACIGS solar cell with a TBC. The JV (and EQE) parameters of all samples are summarized in Table 1.

The JV analysis presented in Figure 4 (and Figure S3, Supporting Information) was performed in a forward voltage sweep. We observed that the characteristics changed when sweeping the voltage from positive to negative voltages. Figure 5 shows the JV characteristics of a cell from the sample with the 1  $\mu\text{m}$ -thick absorber (run 4), measured in forward and subsequently (seconds later) in reverse sweep direction. The  $FF$  decreases and  $V_{\text{OC}}$  increases slightly in the reverse sweep, leading to a 0.2–0.6% lower efficiency for the cells of this sample. Thus, it can be expected that the best cell of this study would show an efficiency of about 13.0–13.5% in the field (without antireflection coating) during maximum power point tracking.

Figure 5 also shows the extension of the SCR for  $V = -0.5\text{ V}$  to  $+0.7\text{ V}$ , as determined from CV measurements on the same cell. The  $W_{\text{SCR}}$  values are illustrated for forward and reverse voltage sweeps (corresponding apparent doping profiles in Figure S6, Supporting Information). While  $W_{\text{SCR}}$  matches the absorber thickness for  $V \leq 0\text{ V}$  in both cases, it is significantly lower for



**Figure 5.** JV characteristics of a cell with a 1  $\mu\text{m}$ -thick absorber (run 4), measured in forward and reverse voltage sweep (left y-axis). The corresponding extension of the SCR (deduced from CV measurements) for different voltage biases and sweep directions is shown as well (right y-axis).

positive voltages in the reverse sweep. Notably, this difference disappears again for  $V \approx 0.7$  V. We suggest that this difference in voltage response causes the observed hysteresis effect in JV. The smaller  $W_{SCR}$  reduces the carrier collection upon reverse V-sweep, especially for  $V \approx 0.25$ – $0.65$  V. Again, this feature signifies the very small diffusion length in the absorber film. It should be noted here that no general trend could be detected for all samples in this study. Some samples actually showed higher efficiencies in reverse sweep, in accordance with earlier studies.<sup>[26]</sup> Taking into account all our earlier works on wide-gap ACIGS solar cells, we exclusively observe such strong JV-hysteresis for very high AAC > 0.6. It is suggested that the charge landscape in the absorber (or potentially also at its interfaces) changes upon the applied voltage, due to the drift of mobile  $Na^+$  ions in the bulk of the ACIGS grains (not grain boundaries). The solubility limit (and also the bulk diffusion constant) of sodium in the chalcopyrite lattice increases with substantial Ag-alloying,<sup>[76]</sup> mainly due to an increase in the lattice parameter  $a$ .<sup>[29]</sup> Thus, the high AAC value used in this study may lead to the pronounced drift of  $Na^+$  ions when an external voltage is applied. Long-term stability testing is advised to investigate potential degradation mechanisms, related to ion drift/migration.

### 2.3. Effect of the Transparent Electrodes on Optical and Resistive Losses

While the 13.6% front- and 8.7% rear-efficiency and the rather low NIR absorbance of about 15% at  $\lambda = 1150$  nm (i.e., Si bandgap) are promising results, both parameters need to be improved to justify any application as a top cell in a tandem device. First of all, the NIR absorption has to be reduced to <5%, since the potential bottom cell (either Si or low-gap ACIGS-based) exhibits a significantly higher efficiency ( $\eta > 20\%$ ) and no photons should be unnecessarily “stolen” from it. Thus, parasitic absorption in the transparent electrodes needs to be minimized.

Figure 6a displays the absorbance spectrum of the sample with the 400 nm-thick absorber, together with the corresponding

spectra of the as-grown IOW film on SLG, the as-grown IOW film after annealing in  $N_2$  for 1 h at  $450^\circ C$  and the IOW film in the final solar cell after mechanically removing all top layers. The rather high absorption of the latter spectrum for  $E > E_{G,ACIGS}$  arises from remaining absorber residuals, which could not be completely removed. The plasma wavelength (maximum in NIR absorption) of the IOW film shifts from  $\lambda \approx 1750$  nm to  $\lambda > 2500$  nm after the temperature stress, in agreement with a significantly reduced free charge carrier absorption in the final device. Here, it does not matter if the IOW is “annealed” in  $N_2$  or during absorber deposition, both layers show very similar A spectra. While the reduction in free electron concentration is beneficial in terms of optical properties, it also leads to the observed (fourfold) increase in  $R_{sheet}$  in the final solar cell ( $R_{sheet} \approx 45 \Omega sq^{-1}$ ), indicating that the mobility is not improved (enough) after annealing to counter this effect. Notably, Koide et al. reported on stable  $n$  values ( $< 2 \times 10^{20} cm^{-3}$ ) and mobility values up to  $120 cm^2 Vs^{-1}$  after annealing up to  $500^\circ C$  when the IOW films are grown polycrystalline at  $200^\circ C$ .<sup>[62]</sup> The IOW is grown at room temperature in this study, leading to X-ray amorphous (or very fine-grained) as-grown films, as measured by X-ray diffraction (XRD). The XRD scans for the (222) reflection (cubic phase, bixbyite-type) of the films grown at room temperature, after annealing (in  $N_2$  and during absorber deposition) and grown at  $350^\circ C$  (on sample holder) can be found in Figure S7, Supporting Information. The annealing as well as the absorber deposition led to a full crystallization of the IOW. This solid-phase crystallization typically leads to a mobility boost for hydrogenated  $In_2O_3:X$  films,<sup>[61]</sup> but also for IOW films without hydrogen when annealed at temperatures up to at least  $250^\circ C$ .<sup>[66]</sup> The strong reduction in conductivity after exposure to higher temperatures than  $250^\circ C$  (here  $\geq 450^\circ C$ ) may be related to the presence of sodium (from the SLG) during crystallization, as was suggested before.<sup>[77]</sup> Also, a tungsten loss upon heating above  $250^\circ C$  cannot be ruled out.

In an attempt to directly grow polycrystalline high- $\mu$  and low- $n$  IOW as in ref. [62], we also deposited films at an elevated set temperature of  $350^\circ C$  (on the sample holder). Indeed, the layers

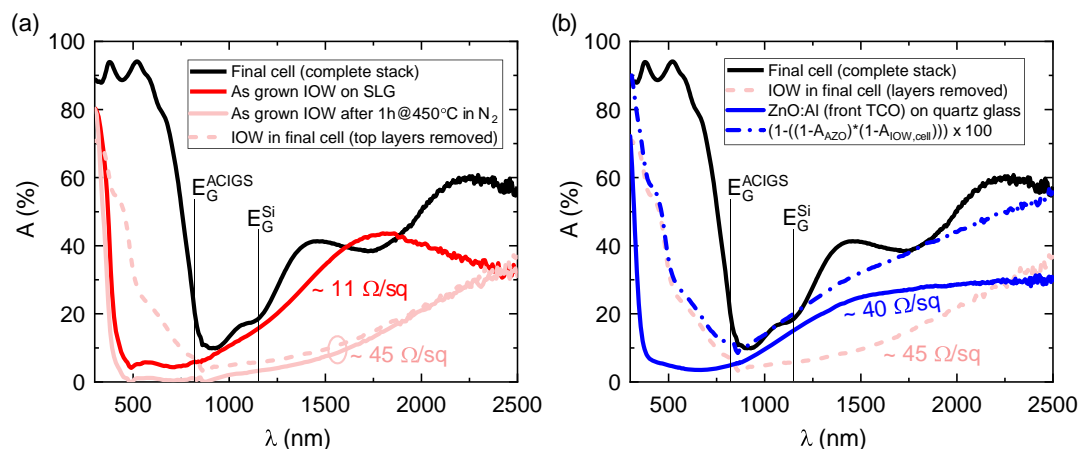


**Figure 6.** a) Absorbance spectra of the complete cell (400 nm-thick absorber, run 1) as well as of the as-grown, annealed (in  $N_2$ ), and final (after absorber deposition and subsequent removal of all top layers) IOW films. b) Absorbance spectra of the complete cell (400 nm-thick absorber, run 1) as well as of the final IOW, the bare ZnO:Al film on quartz glass (used as front TCO), and the combined absorbance of both transparent electrodes. For all TCO films, the corresponding  $R_{sheet}$  values are added as numbers, too.

were slightly more crystalline, but with much smaller grains as compared to the postannealed films. However, those samples showed already a high  $R_{\text{sheet}}$  of  $40 \Omega \text{ sq}^{-1}$  (same thickness) before annealing and degraded significantly after annealing for an hour at  $450^\circ\text{C}$  in  $\text{N}_2$  atmosphere ( $R_{\text{sheet}} > 1 \text{ k}\Omega \text{ sq}^{-1}$ ), which led us to only use the X-ray amorphous IOW films (grown at room temperature) as a TBC for the solar cells in this study. The reason why we could not reproduce the high-quality polycrystalline IOW films reported in ref. [62] is unclear at this stage. A possible explanation could be that a small, unintended  $\text{H}_2$  background pressure in the sputter chamber hampers the IOW crystallization during its deposition, even at elevated temperatures.<sup>[62]</sup> Another possibility is a nonoptimal thermal contact between the metal plate (sample holder) and the SLG, leading to substrate temperatures  $< 200^\circ\text{C}$ . Optimizing the IOW sputter process will be the content of future work. It was for instance shown that the crystallinity of IOW grown at room temperature can be tuned by changing the  $\text{O}_2$  partial pressure<sup>[64]</sup> or sputtering current.<sup>[78]</sup>

Overall, the fourfold increase in  $R_{\text{sheet}}$  means that the resistive loss in the IOW during lateral electron conduction (increasing the series resistance) is the main  $FF$  limitation. The smaller  $R_{\text{sheet}}$  of the AZO top electrode ( $40 \Omega \text{ sq}^{-1}$ ) and the shorter distance to the contacts (see cell configuration in Figure S4c, Supporting Information) lead to a slightly lower impact on the  $FF$ . However, in a final monolithically integrated module, the sheet resistances of the two transparent electrodes are about equally important. In a 2-terminal tandem device, lateral conductivity of the bottom TCO is not as important and it can be made very thin, reducing optical losses.

Figure 6b compares the absorbance spectra of the IOW film in the final cell and of the bare AZO front-TCO on quartz (properties similar to AZO in the final cell). Since the AZO is more doped than the final IOW film, it shows a much higher  $A$  in the NIR region. Thus, it contributes substantially more to the total absorption losses at the bandgap of a possible Si bottom cell. The combined NIR absorption through both transparent electrodes  $A_{\text{comb}}$  can be estimated by:

$$A_{\text{comb}} = 1 - [(1 - A_{\text{AZO}}) \cdot (1 - A_{\text{IOW,cell}})] \quad (1)$$

The corresponding values are added to Figure 6b as well and they match the NIR absorption spectrum of the complete device closely (interference fringes being much less pronounced).

In summary, to improve the NIR transparency of the wide-gap ACIGS solar cells in this work, a front TCO with a lower  $n$  and a higher  $\mu$  (AZO used here:  $n > 3 \times 10^{20} \text{ cm}^{-3}$  and  $\mu \approx 20 \text{ cm}^2 \text{ Vs}^{-1}$ <sup>[79]</sup>) needs to be chosen, such as annealed IOH<sup>[79–82]</sup> or IOW<sup>[63,64]</sup> films, chemical vapor deposited ZnO: B or sputtered Zn-In-O.<sup>[83]</sup> In addition, the conductivity of the TBC should not be compromised by the high-temperature ACIGS deposition, as observed in this work for IOW and in earlier works for IOH.<sup>[58–60]</sup> Since the thermal stability of polycrystalline IOW was proven before,<sup>[62]</sup> our first attempt will be to grow stable polycrystalline IOW films by changing the sputter process parameters. Without thermal  $R_{\text{sheet}}$  degradation, the  $FF$  should approach the values of reference devices on Mo even closer.

To improve the performance at rear illumination, thereby allowing to use the substrate glass as the front glass in the final

top cell/module, passivation of the back contact, and optimization of the GGI grading are required. Otherwise, losses in  $J_{\text{SC}}$  will remain too large to “flip the device.” Furthermore, the carrier collection was improved in this work by choosing close-stoichiometric and high-Ag-containing ACIGS absorbers. For large-scale industrial production, it may be a challenge to keep the composition close-stoichiometric across the entire module area.

Ultimately, to make chalcopyrite-based solar cells a true option as a tandem partner with high-performing bottom cells like Si, the absorber bulk properties (i.e., electron lifetime) need to be improved further to reduce deficits in  $V_{\text{OC}}$  and  $FF$ . Only then, necessary efficiencies  $> 18\%$  can be achieved.

### 3. Conclusion

Efficiencies of up to 13.6% are reached for wide-gap ( $E_{\text{G}} = 1.4\text{--}1.5 \text{ eV}$ ) ACIGS solar cells with low NIR absorption ( $A \approx 15\%$  at  $\lambda = 1150 \text{ nm}$ ), using  $\text{In}_2\text{O}_3\text{:W}$  as a TBC. The  $1 \mu\text{m}$ -thick absorber is completely depleted in charge carriers, i.e.,  $W_{\text{SCR}} = d_{\text{ACIGS}}$ , owing to its close-stoichiometric composition and high silver concentration ( $\text{AAC} \approx 0.8$ ). As a result, carrier collection is almost perfect for front illumination, while at rear illumination  $J_{\text{SC}}$  reaches 62% of the value measured at front illumination. It is suggested that remaining collection losses arise from a combination of back contact recombination (no passivation layer applied here) and a too low drift/diffusion length. Reducing the absorber thickness to  $\leq 450 \text{ nm}$  only leads to improved collection at rear illumination for charge carriers generated very close to the back contact ( $\lambda < 550\text{--}600 \text{ nm}$ ). This implies that the main limitation at rear illumination is back contact recombination, providing hope that the efficiency can be substantially increased via the implementation of passivation structures.

The  $\text{In}_2\text{O}_3\text{:W}$  back electrodes are sputter-deposited at room temperature, resulting in X-ray amorphous films with very low resistivity ( $3.3 \times 10^{-4} \Omega \text{ cm}$ ). The high temperature during absorber formation ( $550^\circ\text{C}$ ) leads to a complete crystallization, a fourfold increase in sheet resistance, and a drastic reduction in NIR absorption. This strongly indicates that the doping density decreases upon crystallization, while the mobility is not increased (at least not by the same factor). In future works, the sputter conditions will be altered in a way that polycrystalline, thermally stable, and low- $n$ /high- $\mu$   $\text{In}_2\text{O}_3\text{:W}$  films can be grown. When those are combined with a front TCO that is more transparent than ZnO:Al (as used here), higher  $FF$ s and even lower NIR absorption can be reached.

### 4. Experimental Section

**Solar Cell Processing:** The solar cells processed in this study were built in the following stack order: SLG/(Mo or IOW)/NaF/ACIGS/CdS/ZnO:Al. The back contact material was either sputter-deposited Mo (320 nm,  $R_{\text{sheet}} \approx 0.7 \Omega \text{ sq}^{-1}$ ) or IOW (300 nm,  $R_{\text{sheet}} \approx 11 \Omega \text{ sq}^{-1}$ ). An  $\text{In}_2\text{O}_3\text{:W}$  compound target (1 wt%  $\text{WO}_3$ ) was used to sputter (radio frequency) the IOW films in an Ar (40 sccm) and  $\text{O}_2$  (0.6 sccm) gas mixture. No alkali diffusion barrier was introduced underneath the back contact. The IOW films were coated with a 5 nm-thick NaF precursor layer, while 12 nm-thick NaF was used for all Mo references.

A three-stage (group I-poor → group I-rich → group I-poor) coevaporation process was applied to grow the ACIGS films at a maximum temperature of 550 °C. The samples in this study stem from 4 deposition runs, leading to similar composition, but different absorber thicknesses, each containing a sample with IOW and Mo (reference) as a back contact. The range of integral metal ratios was  $AAC = 0.79\text{--}0.82$ ,  $GGI = 0.55\text{--}0.59$ ,  $[I]/[III] \approx 0.9\text{--}1.0$ , deduced from cross-calibrated XRF measurements on bare absorbers. Small differences in composition emanated from the lateral distribution of the metal sources in the evaporation chamber. The ratio of the Ag and Cu evaporation rates was kept constant at any time. To implement a bandgap grading toward the back contact, higher Ga and lower In evaporation rates were chosen in the initial growth stages. A heavy alkali postdeposition treatment was not implemented.

After absorber deposition, a 55 nm thick CdS buffer layer was grown via chemical bath deposition at 60 °C. Finally, a ZnO:Al window layer (220 nm;  $R_{\text{sheet}} \approx 40 \Omega \text{ sq}$ ) was sputtered on top. The completed samples with a TBC were sectioned into 16 individual solar cells (area = 0.1 cm<sup>2</sup>) via local, selective removal of the buffer and window layers (etching in HCl), allowed by a photolithography masking process (compare Figure S4c, Supporting Information). Mechanical scribing was used to define solar cells for the Mo reference samples (area = 0.05 cm<sup>2</sup>).

**Material Characterization:** Integral absorber compositions were determined with a Panalytical Epsilon 5 XRF spectrometer. Laterally integrated elemental depth profiles were deduced from GDOES in a Spectrumba Analytik GDA 750HR system (quantification done by matching the integral XRF compositions). Optical characterization ( $R$  &  $T$  measurements) of full solar cell stacks (before cell definition) was conducted in a Perkin Elmer Lambda 900 spectrometer with an integrating sphere. A Zeiss Merlin SEM (acceleration voltage of 5 kV) was used to investigate the solar cell cross-sections. STEM and EDS analyses were performed on a probe-corrected ThermoFisher Scientific Titan Themis 200 XFEG instrument equipped with a super-X detector and operated at 200 kV. The TEM lamella was prepared via a focused ion beam in a Zeiss Crossbeam 550 system, following the lift-out technique. A final milling step at maximum 1 kV ion accelerating voltage was performed on both sides of the lamellae, and no further electron exposure was done during focused ion beam preparation before the TEM analyses. The sheet resistance of the electrodes was measured in a linear 4-point probe configuration. The crystallinity of the IOW films was investigated using a Philips X'Pert diffractometer in  $\Theta/2\Theta$  scanning mode.

**Electro-Optical Characterization of Solar Cells:** The JV (all 16 cells per sample) and EQE (only the best cell for each sample) measurements of completed solar cells were done using home-built setups. To avoid any reflection from the stage surfaces, a highly absorbing black sponge was placed underneath the solar cells with IOW back contacts. The JV characteristics were measured in forward V-sweep at a temperature of 25 °C under illumination by an ELH lamp. For each sample, the light intensity was adjusted to match the  $J_{\text{SC}}$  value at 1 sun irradiance of a calibrated Si reference solar cell. After measuring JV on all solar cells, the EQE was measured only on the best cells for each sample. Since a JV-hysteresis was detected, the characteristics were also measured in reverse V-sweep for selected samples. Capacitance-voltage profiling was conducted from  $V = -0.5$  to  $+0.7$  V at 60 kHz and an amplitude of 25 mV, using an Agilent 4284A precision LCR meter and a Keithley 2401 source meter. A dielectric constant of  $\epsilon_r = 10$  was assumed for the ACIGS material in this study.

## Supporting Information

Supporting Information is available from the Wiley Online Library or from the author.

## Acknowledgements

This work was financially supported by the European Union Program HORIZON (Call: HORIZON-CLS-2021-D3-02, Project ID: 101075626 (SITA)) and the Swedish Energy Agency under the project number

P50992-1, Dnr 2020-009335. A.F.V. acknowledges the Fundação para a Ciência e Tecnologia (FCT) through the grant no. 2020.07073.BD.

## Conflict of Interest

The authors declare no conflict of interest.

## Data Availability Statement

The data that support the findings of this study are available from the corresponding author upon reasonable request.

## Keywords

ACIGS, In<sub>2</sub>O<sub>3</sub>:W, silver alloying, tandem device, wide-gap solar cell

Received: June 11, 2024  
Published online: July 8, 2024

- [1] J. Keller, K. Kiselman, O. Donzel-Gargand, N. M. Martin, M. Babucci, O. Lundberg, E. Wallin, L. Stolt, M. Edoff, *Nat. Energy* **2024**, *9*, 46.
- [2] M. A. Contreras, L. M. Mansfield, B. Egaas, J. Li, M. Romero, R. Noufi, E. Rudiger-Voigt, W. Mannstadt, *Prog. Photovolt. Res. Appl.* **2012**, *20*, 843.
- [3] A. S. Brown, M. A. Green, *Phys. E* **2002**, *14*, 96.
- [4] R. K. Kothandaraman, Y. Jiang, T. Feurer, A. N. Tiwari, F. Fu, *Small Methods* **2020**, *4*, 2000395.
- [5] J. Keller, P. Pearson, N. Shariati Nilsson, O. Stolt, L. Stolt, M. Edoff, *Sol. RRL* **2021**, *5*, 2100403.
- [6] S. Siebentritt, U. Rau, *Wide-Gap Chalcopyrites*, Springer-Verlag, Berlin, Heidelberg **2006**.
- [7] S. Hegedus, W. N. Shafarman, *Prog. Photovolt. Res. Appl.* **2004**, *12*, 155.
- [8] B. Huang, S. Chen, H. Deng, L. Wang, M. A. Contreras, R. Noufi, S.-H. Wei, *IEEE J. Photovoltaics* **2014**, *4*, 477.
- [9] J. Pohl, K. Albe, *Phys. Rev. B* **2013**, *87*, 245203.
- [10] C. Spindler, F. Babbe, M. H. Wolter, F. Ehre, K. Santosh, P. Hilgert, F. Werner, S. Siebentritt, *Phys. Rev. Mater.* **2019**, *3*, 090302.
- [11] C. Spindler, D. Regesch, S. Siebentritt, *Appl. Phys. Lett.* **2016**, *109*, 032105.
- [12] S. Lany, A. Zunger, *J. Appl. Phys.* **2006**, *100*, 113725.
- [13] G. Hanna, A. Jasenek, U. Rau, H. W. Schock, *Thin Solid Films* **2001**, *387*, 71.
- [14] G. Hanna, A. Jasenek, U. Rau, H. W. Schock, *Phys. Status Solidi A* **2000**, *179*, 7.
- [15] M. R. Balboul, H. W. Schock, S. A. Fayak, A. A. El-Aal, J. H. Werner, A. A. Ramadan, *Appl. Phys. A* **2008**, *92*, 557.
- [16] M. Raghuvanshi, E. Cadel, P. Pareige, S. Duguay, F. Couzinie-Devy, L. Arzel, N. Barreau, *Appl. Phys. Lett.* **2014**, *105*, 013902.
- [17] S.-H. Wei, A. Zunger, *J. Appl. Phys.* **1995**, *78*, 3846.
- [18] M. Gloeckler, J. R. Sites, *Thin Solid Films* **2005**, *480–481*, 241.
- [19] M. Turcu, O. Pakma, U. Rau, *Appl. Phys. Lett.* **2002**, *80*, 2598.
- [20] S. Chen, X. G. Gong, S. H. Wei, *Phys. Rev. B* **2007**, *75*, 205209.
- [21] D. Huang, J. W. Jiang, J. Guo, Y. J. Zhao, R. Chen, C. Persson, *Mater. Sci. Eng. B* **2018**, *236–237*, 147.
- [22] J. Keller, K. V. Sopiha, O. Stolt, L. Stolt, C. Persson, J. J. S. Scragg, T. Törndahl, M. Edoff, *Prog. Photovolt. Res. Appl.* **2020**, *28*, 237.
- [23] G. M. Hanket, J. H. Boyle, W. N. Shafarman, in *34th IEEE Photovolt. Spec. Conf.*, Philadelphia, June **2009**, p. 001240.

- [24] T. Nakada, K. Yamada, R. Arai, H. Ishizaki, N. Yamada, *MRS Proc.* **2005**, 865, F11.1.
- [25] T. Umehara, F. Zulkifly, K. Nakada, A. Yamada, *Jpn. J. Appl. Phys.* **2017**, 56, 08MC09.
- [26] J. Keller, L. Stolt, K. V. Sopiha, J. K. Larsen, L. Riekehr, M. Edoff, *Sol. RRL* **2020**, 4, 2000508.
- [27] J. K. Larsen, O. Donzel-Gargand, K. V. Sopiha, J. Keller, K. Lindgren, C. Platzer-Björkman, M. Edoff, *ACS Appl. Energy Mater.* **2021**, 4, 1805.
- [28] J. Keller, H. Aboufadel, L. Stolt, O. Donzel-Gargand, M. Edoff, *Sol. RRL* **2022**, 6, 2200044.
- [29] J. H. Boyle, B. E. McCandless, W. N. Shafarman, R. W. Birkmire, *J. Appl. Phys.* **2014**, 115, 223504.
- [30] J. Boyle, G. Hanket, W. N. Shafarman, in *34th IEEE Photovolt. Spec. Conf.* Philadelphia, June **2009**, p. 001349.
- [31] P. Pearson, J. Keller, L. Stolt, O. Donzel-Gargand, C. Platzer Björkman, *Sol. RRL* **2024**, 8, 2400220.
- [32] J. Keller, L. Stolt, T. Törndahl, M. Edoff, *Sol. RRL* **2023**, 7, 2300208.
- [33] M. J. Shin, S. Park, A. Lee, S. J. Park, A. Cho, K. Kim, S. K. Ahn, J. Hyung Park, J. Yoo, D. Shin, I. Jeong, J. H. Yun, J. Gwak, J. S. Cho, *Appl. Surf. Sci.* **2021**, 535, 147732.
- [34] T. Nakada, Y. Hirabayashi, T. Tokado, D. Ohmori, T. Mise, *Sol. Energy* **2004**, 77, 739.
- [35] R. Caballero, S. Siebentritt, K. Sakurai, C. A. Kaufmann, M. C. Lux-Steiner, in *Conf. Rec. 2006 IEEE 4th World Conf. Photovolt. Energy Conversion, WCPEC-4*, May **2006**, Hawaii, p. 479.
- [36] W. Ohm, W. Riedel, U. Aksünger, D. Greiner, C. A. Kaufmann, M. C. Lux-Steiner, S. Gledhill, in *2015 IEEE 42nd Photovolt. Spec. Conf. PVSC 2015*, New Orleans, June **2015**, p. 1.
- [37] F. Mollica, M. Jubault, F. Donsanti, A. Loubat, M. Bouttemy, A. Etcheberry, N. Naghavi, *Thin Solid Films* **2017**, 633, 202.
- [38] M. Mazzer, S. Rampino, G. Spaggiari, F. Annoni, D. Bersani, F. Bissoli, M. Bronzoni, M. Calicchio, E. Gombia, A. Kingma, F. Pattini, E. Gilioli, *Sol. Energy Mater. Sol. Cells* **2017**, 166, 247.
- [39] M. J. Shin, J. H. Jo, A. Cho, J. Gwak, J. H. Yun, K. Kim, S. K. Ahn, J. H. Park, J. Yoo, I. Jeong, B. H. Choi, J. S. Cho, *Sol. Energy* **2019**, 181, 276.
- [40] M. J. Shin, A. Lee, A. Cho, K. Kim, S. K. Ahn, J. H. Park, J. Yoo, J. H. Yun, J. Gwak, D. Shin, I. Jeong, J. S. Cho, *Nano Energy* **2021**, 82, 105729.
- [41] N. Cavallari, F. Pattini, S. Rampino, F. Annoni, M. Barozzi, M. Bronzoni, E. Gilioli, E. Gombia, C. Maragliano, M. Mazzer, G. Peponi, G. Spaggiari, R. Fornari, *Appl. Surf. Sci.* **2017**, 412, 52.
- [42] N. Hamada, T. Nishimura, J. Chantana, Y. Kawano, T. Masuda, T. Minemoto, *Sol. Energy* **2020**, 199, 819.
- [43] J. Chantana, H. Arai, T. Minemoto, *J. Appl. Phys.* **2016**, 120, 045302.
- [44] T. Schneider, R. Scheer, in *36th Eur. Photovolt. Sol. Energy Conf. Exhib.*, Marseille, September **2019**, p. 684.
- [45] T. Schneider, T. Hölscher, H. Kempa, R. Scheer, in *37th Eur. Photovolt. Sol. Energy Conf. Exhib.*, September **2020**, p. 621.
- [46] Y. S. Son, H. Yu, J. K. Park, W. M. Kim, S. Y. Ahn, W. Choi, D. Kim, J. H. Jeong, *J. Phys. Chem. C* **2019**, 123, 1635.
- [47] M. Saifullah, D. Kim, J. S. Cho, S. J. Ahn, S. J. Ahn, J. H. Yun, H. S. Lee, J. H. Park, *J. Mater. Chem. A* **2019**, 7, 21843.
- [48] A. Jeong, J. M. Choi, H.-J. Lee, G.-Y. Kim, J.-K. Park, W. M. Kim, S. Kuk, Z. Wang, D. J. Hwang, H. Yu, J. Jeong, *Prog. Photovolt. Res. Appl.* **2022**, 30, 713.
- [49] Y. Li, G. Yin, Y. Gao, T. Köhler, J. Lucassen, M. Schmid, *Sol. Energy Mater. Sol. Cells* **2021**, 223, 110969.
- [50] Y. Li, G. Yin, M. Schmid, *Sol. Energy Mater. Sol. Cells* **2022**, 234, 111431.
- [51] T. Schneider, C. Dethloff, T. Hölscher, H. Kempa, R. Scheer, *Prog. Photovolt. Res. Appl.* **2022**, 30, 191.
- [52] A. Mavlonov, J. Chantana, T. Nishimura, Y. Kawano, M. Inoue, N. Hamada, T. Masuda, T. Minemoto, *Sol. Energy* **2020**, 211, 725.
- [53] A. Mavlonov, T. Nishimura, J. Chantana, Y. Kawano, T. Minemoto, *Appl. Phys. Lett.* **2021**, 119, 103903.
- [54] J. H. Choi, K. Kim, Y. J. Eo, J. H. Park, J. Gwak, S. K. Ahn, A. Cho, S. Ahn, J. S. Cho, K. Shin, K. Yoon, S. H. Kong, J. Yoo, *Vacuum* **2015**, 120, 42.
- [55] D. Abou-Ras, G. Kosterz, D. Bremaud, M. Kälin, F. V. Kurdesau, A. N. Tiwari, M. Döbeli, *Thin Solid Films* **2005**, 480–481, 433.
- [56] D. Kim, S. S. Shin, Y. Jo, S. M. Lee, S. K. Ahn, J. S. Cho, J. H. Yun, H. S. Lee, J. H. Park, *Adv. Sci.* **2022**, 9, 2105436.
- [57] C. Rath, Y. Gao, T. Koehler, M. Schmid, *Adv. Mater. Interfaces* **2024**, 11, 2400085.
- [58] J. Keller, W.-C. Chen, L. Riekehr, T. Kubart, T. Törndahl, M. Edoff, *Prog. Photovolt. Res. Appl.* **2018**, 26, 846.
- [59] J. Keller, N. Shariati Nilsson, A. Aijaz, L. Riekehr, T. Kubart, M. Edoff, T. Törndahl, *Prog. Photovolt. Res. Appl.* **2018**, 26, 159.
- [60] J. Keller, L. Stolt, O. Donzel-Gargand, T. Kubart, M. Edoff, *Sol. RRL* **2022**, 6, 2200401.
- [61] T. Koida, H. Fujiwara, M. Kondo, *Jpn. J. Appl. Phys.* **2007**, 46, 685.
- [62] T. Koida, Y. Ueno, *Phys. Status Solidi A* **2021**, 218, 2000487.
- [63] Z. Lu, F. Meng, Y. Cui, J. Shi, Z. Feng, Z. Liu, *J. Phys. D: Appl. Phys.* **2013**, 46, 075103.
- [64] C. Han, Y. Zhao, L. Mazzarella, R. Santbergen, A. Montes, P. Procel, G. Yang, X. Zhang, M. Zeman, O. Isabella, *Sol. Energy Mater. Sol. Cells* **2021**, 227, 111082.
- [65] S. Aikawa, P. Darmawan, K. Yanagisawa, T. Nabatame, Y. Abe, K. Tsukagoshi, *Appl. Phys. Lett.* **2013**, 102, 102101.
- [66] T. Gan, J. Li, L. Wu, J. Zhang, X. Hao, Q. Zhang, R. Li, W. Shi, *Mater. Sci. Semicond. Process* **2022**, 138, 106257.
- [67] S. C. Yang, T. Y. Lin, M. Ochoa, H. Lai, R. Kothandaraman, F. Fu, A. N. Tiwari, R. Carron, *Nat. Energy* **2023**, 8, 40.
- [68] K. V. Sopiha, J. K. Larsen, O. Donzel-Gargand, F. Khavari, J. Keller, M. Edoff, C. Platzer-Björkman, C. Persson, J. J. S. Scragg, *J. Mater. Chem. A* **2020**, 8, 8740.
- [69] E. Cadet, N. Barreau, J. Kessler, P. Pareige, *Acta Mater.* **2010**, 58, 2634.
- [70] J. Lehmann, S. Lehmann, I. Laueremann, T. Rissom, C. A. Kaufmann, M. C. Lux-Steiner, M. Bär, S. Sadewasser, *J. Appl. Phys.* **2014**, 116, 233502.
- [71] J. H. Boyle, B. E. McCandless, G. M. Hanket, W. N. Shafarman, *Thin Solid Films* **2011**, 519, 7292.
- [72] H. Simchi, B. McCandless, W. Shafarman, K. Kim, J. Boyle, R. Birkmire, in *37th IEEE Photovolt. Spec. Conf.*, Washington, June **2011**, p. 000041.
- [73] J. C. Mikkelsen, *Mater. Res. Bull.* **1977**, 12, 497.
- [74] I. A. Ivashchenko, I. V. Danyliuk, I. D. Olekseyuk, V. V. Halyan, *J. Solid State Chem.* **2014**, 210, 102.
- [75] J. Keller, N. Martin, O. Donzel-Gargand, K. Kiselman, U. Zimmermann, L. Stolt, C. Platzer-Björkman, M. Edoff, *Sol. RRL* **2024**, 8, 2301018.
- [76] H. Aboufadel, K. V. Sopiha, J. Keller, J. K. Larsen, J. J. S. Scragg, C. Persson, M. Thuvander, M. Edoff, *ACS Appl. Mater. Interfaces* **2021**, 13, 7188.
- [77] X. Li, W. Liu, W. Zhao, S. Huang, W. Huang, J. Shi, A. Han, J. Li, H. Chen, L. Zhang, F. Meng, Z. Liu, *Sol. Energy Mater. Sol. Cells* **2021**, 233, 111387.
- [78] Y. Li, W. Wang, J. Zhang, R. Wang, *Rare Met.* **2012**, 31, 158.
- [79] J. Keller, A. Aijaz, F. Gustavsson, T. Kubart, L. Stolt, M. Edoff, T. Törndahl, *Sol. Energy Mater. Sol. Cells* **2016**, 157, 757.

- [80] J. Keller, L. Stolt, M. Edoff, T. Törndahl, *Phys. Stat. Solidi A* **2016**, *213*, 1541.
- [81] J. Keller, J. Lindahl, M. Edoff, L. Stolt, T. Törndahl, *Prog. Photovolt. Res. Appl.* **2016**, *24*, 102.
- [82] T. Jäger, Y. E. Romanyuk, S. Nishiwaki, B. Bissig, F. Pianezzi, P. Fuchs, C. Gretener, M. Döbeli, A. N. Tiwari, *J. Appl. Phys.* **2015**, *117*, 205301.
- [83] M. Morales-Masis, S. De Wolf, R. Woods-Robinson, J. W. Ager, C. Ballif, *Adv. Electron. Mater.* **2017**, *3*, 1600529.